



# Measurements of the local equivalence ratio and its impact on the thermochemical state in laminar partially premixed boundary layer flames

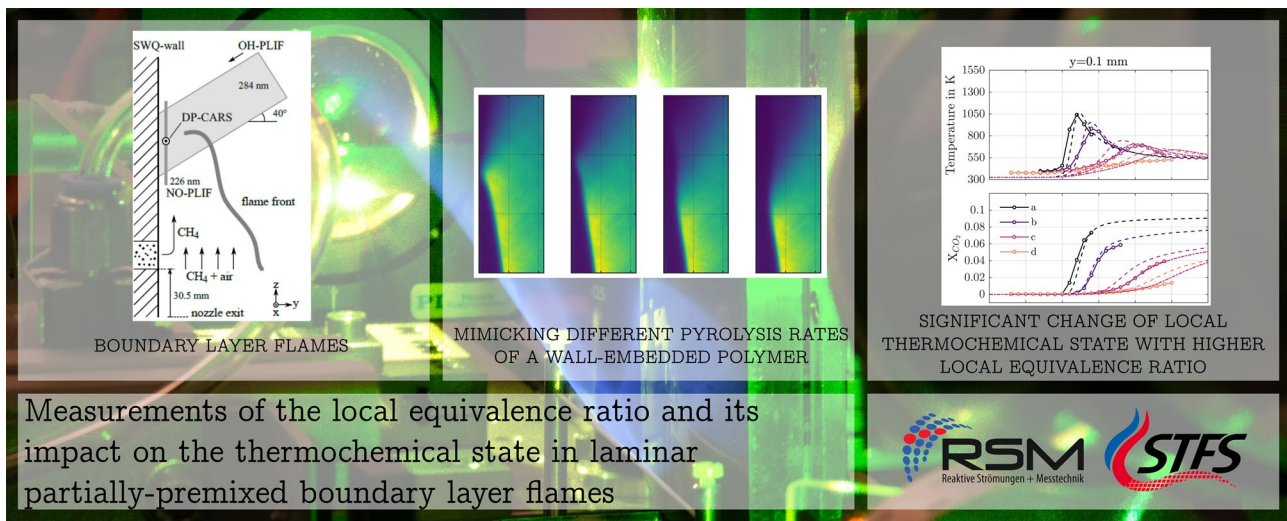
M. Greifenstein<sup>1</sup> · F. Zentgraf<sup>1</sup> · P. Johe<sup>1</sup> · B. Boehm<sup>1</sup> · M. Steinhausen<sup>2</sup> · C. Hasse<sup>2</sup> · A. Dreizler<sup>1</sup>

Received: 29 June 2023 / Revised: 10 October 2023 / Accepted: 18 November 2023 / Published online: 17 December 2023  
© The Author(s) 2023

## Abstract

Local fuel–air equivalence ratios, gas phase temperature and CO<sub>2</sub> mole fractions were measured by a combination of laser-induced fluorescence of nitric oxide used as a tracer and dual-pump coherent anti-Stokes Raman spectroscopy in a vertically oriented partially premixed boundary layer flame under laminar flow conditions. By embedding a secondary effusive fuel inlet into the temperature-controlled wall of a sidewall-quenching configuration, different pyrolysis rates of a wall-embedded polymer are mimicked with reduced chemical complexity and well-controlled boundary conditions. The resulting boundary layer flames were investigated experimentally and numerically. The simulation results and measurements show a very good agreement on the complex interplay between local mixing and heat losses, even though inhomogeneities of the wall inlet complicate the comparison of data. Local equivalence ratios upstream of the reaction zone reach values of up to  $\Phi = 2$ . Under these conditions, a clear quenching location could not be identified based on the experimental data. A significant trend toward lower temperatures and CO<sub>2</sub> mole fractions with increasing amount of secondary fuel was found in the thermochemical state close to the temperature-controlled wall, downstream of the effusive inlet.

## Graphical abstract



Measurements of the local equivalence ratio and its impact on the thermochemical state in laminar partially-premixed boundary layer flames



## 1 Introduction

In fire research partially or non-premixed boundary layer flames are canonical configurations (Drysdale 2011). In buoyancy-driven flows, the orientation (vertical, horizontal

top (Ceiling Fire)/bottom (Floor Fire), inclined) of boundary layer flames is important (Zhou and Fernandez-Pello 1992, 1993), whereas the differences decrease with increasing intensity of a forced convection (Zhou and Fernandez-Pello 1992). Boundary layer flames are divided into quasi-stationary, statistically stationary (turbulent), and dynamic, the latter often focusing on flame propagation dynamics. Boundary layer flames further depend on the wall material and type of fuel release (Ren et al. 2016). A distinction is made between passive and active walls. For passive walls, when oriented vertically, fuel addition to form a boundary layer flame often occurs from below through impregnated wicks or as in De Ris et al. (2003), Hirano (1972), and Hirano and Kanno (1973) through a porous plate. For active walls, either a porous sintered structure or a combustible material such as a polymer is embedded into the wall. For combustible wall materials such as polymers, transport processes between gas and condensed phases as well as transport and reaction processes in each of the two phases are process-determining. In the condensed phase, these processes include pyrolysis, which releases combustible gases, and ignition with subsequent formation of a boundary layer flame. These transport and reaction processes determine the mass burning rate (Orloff et al. 1977), the heat release rate and thus the intensity of a near-surface combustion (Singh and Gollner 2015). They depend on the flow regime, which can be laminar or turbulent.

Boundary layer flames have been studied for a long time. In early investigations, such as in Emmons (1956), Krishnamurthy and Williams (1973), the goal was a theoretical description of a stationary, laminar boundary layer flame, assuming a number of simplifications. Theoretical approaches were increasingly supplemented by numerical simulations in addition to experimental investigations (Zhou and Fernandez-Pello 1993), and the problem was extended to flame spread (Annamalai and Sibilkin 1979). Based on RANS approaches, buoyancy-driven, statistically stationary boundary layer flames were already simulated in the 1970s for non-combustible (Kennedy and Plumb 1977) as well as combustible walls (Tamanini 1979). Examples of spreading flame simulations can be found in Consalvi et al. (2005, 2008). With increasing availability of computational resources, DNS calculations of buoyancy-driven laminar boundary layer flames with (Mell and Kashiwagi 1998; Shih and Tien 2000; Mell and Kashiwagi 2000; Nakamura et al. 2002; Shih and James 2003) and without flame spreading (Ananth et al. 2003; Raghavan et al. 2009) were published with simplified assumptions on the chemical reactions. This allowed flame–wall interactions to be investigated, although

these remained limited to small scales. Surprisingly, there are only few LES studies on boundary layer flames (Wang et al. 2002; Ren et al. 2016). This is because LES of boundary layer flames require high resolution of the computational grid near the wall to resolve the relevant scales. Often Reynolds numbers are in a range where classical boundary layer theory does not apply, and a multiphysics multiphase phenomenon of high complexity is present.

This brief literature review shows that the focus of previous investigations has been particularly on global features, such as mass burning rates, heat release rates and flame spreading. Thermochemical states similar to the interaction of premixed flames and walls (Zentgraf et al. 2022b) have not been investigated. Knowledge of local equivalence ratios, local gas temperature, and chemical species concentrations were measured rarely. However, this detailed information is important to gain a better understanding of the boundary layer flame's microstructure and to provide data to validate scale-resolved numerical simulations.

The aim of this study<sup>1</sup> is to investigate local thermochemical states in a canonical, vertically oriented boundary layer flame under laminar flow conditions. Based on the configuration presented in Zentgraf et al. (2022b), the pyrolysis of a polymer is simulated by the outflow of methane at low speeds from a porous sintered structure embedded into the vertically oriented wall. Different pyrolysis rates are mimicked by varying the methane mass flow rates. Local mixing states are measured via NO-Tracer-PLIF (Greifenstein and Dreizler 2021a) simultaneously with gas temperatures and CO<sub>2</sub> mass fractions using DP-CARS (Zentgraf et al. 2022b). In addition, the location of reaction zones is visualized via OH-PLIF. To gain a deeper insight into the process, the experimental investigations are accompanied by numerical simulations.

## 2 Experimental and numerical setup

### 2.1 Burner facility

The SWQ burner facility used in this study for investigating partially premixed boundary layer flames interacting with a temperature stabilized wall is shown in Fig. 1.

The burner is a well-established reference case that has been extensively studied experimentally and numerically in previous publications, e.g., Zentgraf et al. (2022b), Steinhäusen et al. (2022), Zentgraf et al. (2022a), Kosaka et al. (2018), Kosaka et al. (2020), Steinhäusen et al. (2021) Premixed air and fuel are fed into the plenum ① through eight ports around the perimeter of the rectangular body. The

<sup>1</sup> This article contains text and figures of the dissertation of Zentgraf (2022) published under Creative Commons (2013).

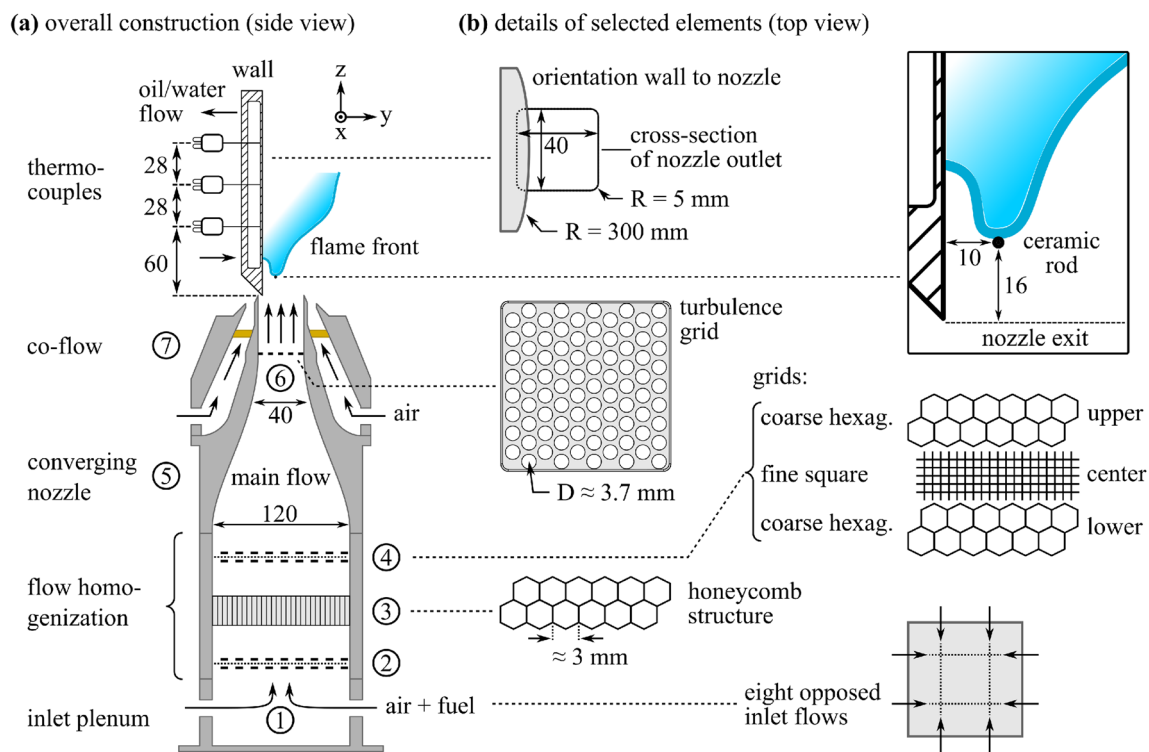


**Fig. 1** Schematic of the SWQ burner: **a** overall construction; **b** selected details. All dimensions without units are given in millimeters. Figure taken from Zentgraf (2022) published under Creative Commons (2013)

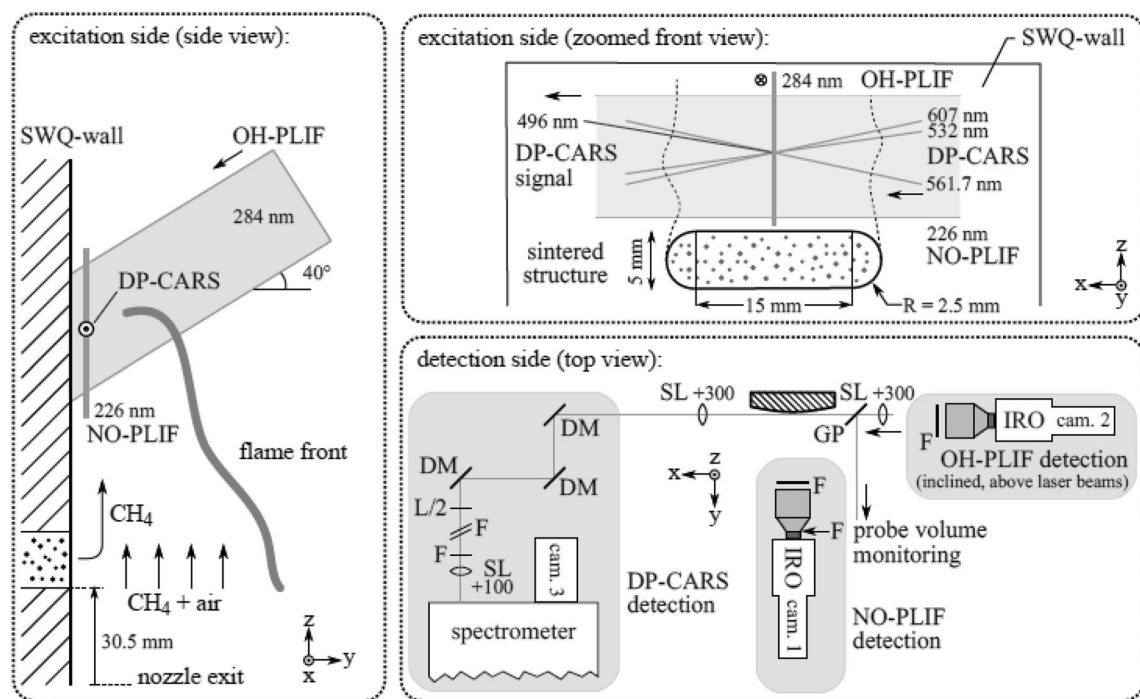


**Fig. 2** Laser diagnostics setup with the excitation and modified quenching wall configuration shown in a side as well as front view and the detection side in a top view. Numbers at spherical lenses

denote focal length in millimeters. Figure taken from Zentgraf (2022) published under Creative Commons (2013)

**Table 1** List of operating conditions of boundary layer flames used in this study

Case	a	b	c	d
$\dot{V}$	0 Lh <sup>-1</sup>	2 Lh <sup>-1</sup>	3.5 Lh <sup>-1</sup>	4.5 Lh <sup>-1</sup>

inflow passes two fine square meshes placed between two coarse hexagonal meshes (② and ④, width  $\approx 5$  mm) and a honeycomb structure (③, height 25 mm, distance between opposed edges  $\approx 3$  mm). A Morel-type nozzle (⑤) with a contraction ratio of 9 reduces the inner cross section from  $120 \times 120$  mm<sup>2</sup> to  $40 \times 40$  mm<sup>2</sup> to ensure a nearly top-hat velocity profile at the nozzle exit. Optionally, a turbulence grid (⑥) can be installed between the Morel nozzle and a short straight section before the flow exits the burner outlet nozzle. For this study, the turbulence grid was removed to allow measurements of the laminar case. To shield the flow from the environment and to avoid shear effects at the nozzle edges, a co-flow (⑦) with the same bulk outlet velocity as the main flow through the burner is used. The co-flow is fed using dry air and passes a sintered bronze plate for homogenization. A cylindrical ceramic rod with 1 mm diameter is mounted on a vertically adjustable stage to allow adjusting the quenching height in this experiment to force the interaction with the secondary fuel inlet at a desired height, see Fig. 2. The lateral distance between the quenching wall and the ceramic rod is 10 mm.

After ignition, a V-flame is stabilized at the ceramic rod featuring a free (quasi-adiabatic) flame branch and a branch interacting with the quenching wall and the secondary fuel inlet. To enable laser-based measurements very close to the wall, the quenching wall has a curvature in the xy-plane with a radius of 300 mm. The quenching wall is temperature stabilized to 60 °C using an adjustable cooling water flow through internal cooling channels and temperature monitoring using three type-K thermocouples along the central axis at different heights. The tips of the thermocouples are contacted with the wall approximately 200–400  $\mu\text{m}$  below the flame-facing surface.

In contrast to previous studies, the quenching wall features an additional fuel inlet port to force partial-premixing in the vicinity of the wall. The flow rate of this second fuel supply is rather small to mimic the pyrolysis of a polymer in a cross-flow near an ongoing combustion process. For this purpose, a  $20 \times 5$  mm<sup>2</sup> (corner radius 5 mm, active area 95 mm<sup>2</sup>) porous sintered bronze inlay is mounted flush with the wall 30.5 mm above the nozzle exit, see Fig. 2.

Within this study, four different CH<sub>4</sub> flow rates<sup>2</sup> in the range of 0–4.5 Lh<sup>-1</sup> were fed to the secondary fuel inlet

<sup>2</sup> If not otherwise noted, volumetric flow rates are given at normal conditions.

leading to effusive penetration of pure fuel into the premixed main flow, see Table 1 for a definition of cases used in this study. With the main flow operating at stoichiometric conditions, i.e.,  $\Phi = 1$ , partial premixing is limited to locally fuel-rich mixtures. The bulk outlet velocity of the secondary fuel ranges from 0.006 to 0.014 ms<sup>-1</sup>. The velocity ratio between the highest setpoint for secondary fuel inflow and primary main flow is  $\approx 0.0056$ , using the bulk outlet velocity of 2.12 ms<sup>-1</sup> for the primary flow. The aim was to achieve very low penetration depths—as to be expected for a pyrolyzing wall-embedded polymer—as well as minimal disturbance of the (isothermal) main flow and rapid mixing in the boundary layer of the quenching wall. However, even though this ratio appears to be negligible at first glance, Stroh et al. (2016) found a uniformly blowing fluid with  $0.005 \cdot U_\infty$  to lead to a thickening of the boundary layer. Consequently, an influence on the local near wall flow field, flame topology and thermochemistry is to be expected.

The burner was operated with a stoichiometric ( $\Phi = 1$ ) CH<sub>4</sub>-air mixture at a Reynolds number of  $\approx 5900$ , based on the hydraulic diameter of the nozzle and the bulk outlet velocity calculated from the volumetric flow rates. All mass flows entering the burner are controlled using individual calibrated thermal mass flow controllers. From calibration measurements, the resulting uncertainty of the equivalence ratio is determined to be  $\Delta\Phi = 0.01$ . The entire burner assembly is mounted on a 3-axis-traversing stage to allow measurements at different near wall locations.

## 2.2 Numerical simulation

The numerical setup used in this study is the same as has been used by Steinhausen et al. (2022). For this reason, only a brief description is given in this publication and the reader is referred to the cited literature.

The domain is discretized in a uniform rectilinear grid with 50  $\mu\text{m}$  grid spacing, and it extends 40 mm in vertical and 6 mm in wall-normal direction. The inlet of the primary flow is modeled using a parabolic velocity profile. To stabilize the flame, hot exhaust gases are injected in a 0.5 mm wide area. To compensate the density difference, the velocity in this area is increased by a factor of 2.244. The outlets of the domain use a zero gradient boundary condition for enthalpy, species and velocity and a Dirichlet boundary condition for pressure. A no-slip boundary condition was used for the temperature stabilized wall (333 K). For the secondary fuel inlet in the wall, a zero gradient boundary condition for pressure is used and the inflow velocity is assumed to be uniform over the surface of the inlet. Species are modeled with a Robin boundary condition. Simulations were carried out using an in-house solver with fully resolved transport and chemistry based on OpenFOAM (v2006). Diffusion is modeled using a mixture-averaged transport model with a

correction velocity (Curtiss and Hirschfelder 1949; Coffee and Heimerl 1981). For the chemical source terms, the GRI-Mech 3.0 reaction mechanism was used (Smith et al. 2011).

## 2.3 Diagnostics

Within this study, dual-pump coherent anti-Stokes Raman spectroscopy (DP-CARS) is combined with planar laser-induced fluorescence of the hydroxyl radical (OH-PLIF) and nitric oxide (NO-PLIF) to measure the local temperature,  $\text{CO}_2$  mole fraction together with the instantaneous location of the flame front and the local equivalence ratio. The following subsections present details on the underlying measurement techniques.

### 2.3.1 NO-PLIF

To investigate mixing between the main flow and secondary fuel, NO calibration gas was seeded to the secondary fuel (10000 ppm<sub>v</sub>) and the main flow (150 ppm<sub>v</sub>). NO was chosen as a tracer due to its high thermal stability and slow reaction kinetics (Skalska et al. 2010), high signal-to-noise ratios (SNR) and well-known spectroscopic properties (Bessler et al. 2002; Sadanandan et al. 2012a; Paul 1997). The additional seeding of the main flow serves a twofold purpose: (a) it allows to extract the energy profile in the laser light sheet in areas with constant seeding density and temperature and (b) allows an assessment of the calibration uncertainty and absorption effects. The local equivalence ratio is derived based on a calibration, where various mixtures with equivalence ratios  $\Phi \in [1, 2]$  were established using calibrated thermal mass flow controllers. For calibration, the mixture was fed into a pipe (4 mm inner diameter) with a fine mesh at the outlet for a homogeneous outflow. Measurements within the core of the jet were used to calibrate the LIF signal. The calibration measurements were taken with the same settings and on the same day as the measurements at the SWQ burner.

Even though the measurement of local equivalence ratio is calibration based and thus the excitation scheme for NO-PLIF is in principle arbitrary, it is tremendously helpful to choose a transition for excitation, where the resulting LIF signal is nearly linear with the quantity of interest. This greatly reduces uncertainties in the evaluation. The line selection procedure is similar to the approach presented by Greifenstein and Dreizler (2021a). In short, LIF excitation spectra were simulated using LifSIM (Bessler et al. 2003) with quenching data from Settersten et al. (2009) for various theoretical mixtures that were also used for the calibration measurements. The simulation was performed in the wavelength range 225.5–226.8 nm and accounted for the measured laser linewidth (High Finesse, WSU-30) and the detection filters used in the experiment (Schott UG5,

Semrock LP02-224R). From this simulation, it was found that the overlapping  $Q_1(2.5) + P_{21}(2.5) + Q_1(3.5) + P_{21}(3.5)$  transitions in the (0,0) vibrational band of the  $A^2\Sigma^+ \leftarrow X^2\Pi$  electronic system near  $44,197.5 \text{ cm}^{-1}$  yield a promising compromise between linearity to the local equivalence ratio and SNR. These transitions were excited with the frequency tripled output of a tunable dye laser (Sirah, PrecisionScan) operated with Pyridine I dissolved in ethanol, which was optically pumped using a frequency doubled pulsed Nd:YAG laser (Spectra Physics, GCR-4) running at 10 Hz repetition rate. The dye laser fundamental frequency and linewidth were measured with a wavemeter (HighFinesse, WSU-30) to ensure long-term stability and validity of the calibration. The maximum pulse energy near 226 nm was approximately 10 mJ at the laser exit.

The initially round beam was expanded in z-direction into a sheet using a cylindrical telescope ( $f = -50 \text{ mm}$ ,  $f = 200 \text{ mm}$ ) and focused in y-direction ( $f = 500 \text{ mm}$ ) into the measurement volume. The lightsheet was  $\approx 8 \text{ mm}$  in height and  $\approx 250 \mu\text{m}$  in thickness at the beam waist ( $1/e^2$ ). Pulse energies were reduced to 2.5 mJ to stay within the linear limits of LIF. The latter was verified by an energy scan in the calibration gas by varying the UV energy output using a half-wave retardation plate in front of the second harmonic generation crystal of the tunable dye laser. For this verification, a pyro-electric energy meter (Coherent, EnergyMax J-10-MT 10 kHz) was placed in a partial reflection of one of the lenses to provide a linear energy reference for the measured LIF signal during the energy scan. The lightsheet is guided into the field of view using high-reflective dielectric mirrors. The orientation was chosen parallel to the wall to avoid excessive scattering of radiation at 226 nm, see the next paragraph for details regarding the suppression of scattered laser radiation.

To detect the signal, a CCD camera (LaVision, Imager E-Lite 1.4M) equipped with a UV-sensitive image intensifier (LaVision, low speed IRO) in combination with a 100 mm UV-lens at  $f/2.8$  (Sodern, Cerco 2178) was used. Choosing a detection scheme for near-wall NO-LIF measurements is challenging, as the separation between the (0,0) vibrational band for excitation and emission in the (0,1) band is only  $\approx 10 \text{ nm}$ . It is desirable to choose a broadband detection of the NO-LIF signal between 235–270 nm for optimal SNR. However, this requires a very steep long pass filter to block the laser radiation, especially considering the finite collection angle of the used optics which one naturally aims to maximize. At  $0^\circ$  angle of incidence and parallel light, the used filter (Semrock, LP02-224R) provides  $> \text{OD}4$  at 226 nm,  $> 50\%$  transmission at 234 nm and  $> 80\%$  transmission for wavelength  $> 244 \text{ nm}$ . However, due to the limited size (1" diameter), the filter was placed between the detection lens and the photocathode of the intensifier in order not to limit the effective aperture of the detection

system. Accounting for the resulting finite cone half angle of  $\approx 17^\circ$ , blocking at laser radiation wavelength is reduced to  $\approx OD2$ , which proved to be insufficient for wall-normal measurements even including the additional Schott UG-5 filter. These filter characteristics have been simulated using Semrock's MyLight filter modeling tool.<sup>3</sup>

The detection systems were operated at double the repetition rate of the laser systems, allowing to use the ensemble average of every second frame for background correction. Additionally, the individual images were corrected for the inhomogeneous energy distribution in the laser light sheet by referencing to the mean signal acquired in the non-reacting seeded main flow. As this approach only allows to correct the energy profile for the temporal mean, a residual fluctuation of  $\approx 7\%$  remains which limits the precision of the local equivalence ratio measurement. Absorption effects are accounted for by correcting the LIF signal with an approach similar to the one developed by Heinze et al. (2011) for quantitative OH measurements. Details may also be found in Greifenstein and Dreizler (2021a). In short, the local laser intensity can be extracted from the data itself—implicitly assuming a constant fluorescence quantum yield in the beam-wise direction—when the integral absorption is known. For this particular case, the absorption was not directly measured but can be indirectly inferred using the reference case (a) without additional inflow through the effusive wall inlet. For this case, the signal can be assumed to be spatially constant and a calibration factor for the correction was extracted which results in a horizontally flat profile. This calibration factor in units absorption per count is then used for all cases to correct for absorption effects. The preprocessed images are then converted to a local equivalence ratio by means of cubic interpolation to the calibration curve.

### 2.3.2 OH-PLIF

Qualitative planar laser-induced fluorescence of the OH radical was acquired simultaneously with the other techniques to infer the instantaneous location of the flame front and quenching height, and the impact on the mean OH distribution from partial premixing. The optical setup is similar to previous publications, see, e.g., Zentgraf et al. (2022b). To generate the LIF signal, a frequency doubled narrowband dye laser (Sirah, PrecisionScan) operated with Rhodamine 6G dissolved in ethanol and optically pumped at 10 Hz repetition rate from a commercial pulsed and frequency doubled Nd:YAG laser (Spectra Physics, PIV400) was tuned to  $35210.42\text{ cm}^{-1}$ , corresponding to the  $Q_2(7.5) + Q_1(9.5)$  linepair in the  $A^2\Sigma \leftarrow X^2\Pi(v' = 1 \leftarrow v'' = 0)$  system of OH. The choice of this linepair is motivated by the low dependency

of the Boltzmann factor with respect to temperature, which amounts to  $\approx 10\%$  between 1400 and 2500 K (Heinze et al. 2011). The spacing between the line centers is  $0.44\text{ cm}^{-1}$  (Luque and Crosley 1999), which overlap well when accounting for Doppler broadening ( $\approx 0.26\text{ cm}^{-1}$  at 1800 K), collisional broadening ( $\approx 0.06\text{ cm}^{-1}$  (Atakan et al. 1997)) and the linewidth of the UV beam ( $\approx 0.15\text{ cm}^{-1}$ , calculated from fundamental linewidth measurement using wavemeter WSU-30, High Finesse) even at atmospheric pressure.

The UV beam was formed into a laser light sheet by first expanding it using a spherical telescope ( $f = -40\text{ mm}$ ,  $f = 200\text{ mm}$ ) to adjust the divergence and increase the diameter. Subsequently, the expanded beam was cropped to  $\approx 10\text{ mm}$  in diameter, using an adjustable iris to improve the spatial homogeneity of laser energy within the beam. The sheet was then focused into the measurement volume with a  $f = 300\text{ mm}$  cylindrical lens and expanded in vertical direction with a  $f = -300\text{ mm}$  cylindrical convex lens to obtain a sheet with  $\approx 35\text{ mm}$  height and a waist of  $\approx 220\text{ }\mu\text{m}$  ( $1/e^2$ ). Due to the wall-parallel orientation of the NO measurement volume, the laser beam for OH excitation was guided above the detection system for NO-PLIF and guided into the FWI area at an angle of  $-40^\circ$  with respect to the horizontal axis. The pulse energy was adjusted to  $\approx 0.5\text{ mJ}$  in the measurement volume by using an achromatic half-wave retardation plate in front of the frequency doubling crystal in the laser.

The LIF signal was detected with a combination of a low-speed image intensifier (LaVision, IRO) and an uncooled CCD camera (LaVision, Imager e-Lite 1.4M) equipped with a  $100\text{ mm}/f2.8$  UV transmissive lens (Sodern, Cerco 2178). A  $2 \times 2$  binning was used to improve the signal-to-noise ratio without sacrificing spatial resolution, as the optical performance was limited by the intensifier. The resulting object-plane resolution of a bin was  $\approx 80\text{ }\mu\text{m}$ . The entire field of view (FOV) spanned an area of  $\approx 41\text{ mm} \times 57\text{ mm}$ . A narrow bandpass filter was used to suppress radiation from the laser and to isolate the emission of the (1,1) vibrational band between 311–320 nm to reduce signal trapping (Sadanandan et al. 2012b).

As OH-PLIF is used in this study for a qualitative description, the processing was kept comparably simple. Raw OH data were background corrected using the same strategy as for NO-PLIF before dewarping and conversion to physical coordinates using a dot pattern target. The remaining dominant uncertainties result from fluctuation in the integral pulse energy and spatial inhomogeneity of the laser sheet.

### 2.3.3 Dual-Pump CARS

As the same Dual-Pump CARS setup from Zentgraf et al. (2022b) was recreated for this study, the description is kept short and the reader is referred to the cited publication. The CARS setup was build up as a planar BOXCARS

<sup>3</sup> <https://www.semrock.com/FilterDetails.aspx?id=LP02-224R-25>, accessed: 2022-05-10.

configuration using two narrowband lasers at 532 nm and 561.7 nm for the two pump beams and a custom built modeless broadband dye laser at 607 nm ( $\approx 6$  nm FWHM) to probe ro-vibrational transitions of  $N_2$  near  $2330\text{ cm}^{-1}$  and  $CO_2$  near  $1380\text{ cm}^{-1}$ . All pulsed lasers were operated at 10 Hz. Each beam featured an independent control of pulse energy via a half-wave retardation plate and a polarizing beam splitter as well as Galilean telescopes to match the divergence to ensure coincident foci in the measurement volume (MV). The beams were parallelized on the optical table and focused into the MV with a  $f = 300$  mm plano-convex lens. The resulting MV, as measured with a beam profiler, had a lateral extension of  $\approx 60\text{ }\mu\text{m}$  and a beam-wise extension of  $\approx 2.4$  mm. The lasers were guided into the FWI area parallel to the wall, such that the influence of limited spatial resolution along the principal axis does not influence the data interpretation too severely, as the V-flame is nearly planar and length scales in this direction are assumed to be longer than the measurement volume.

A symmetrically (with respect to the MV) placed  $f = 300$  mm plano-convex lens collimated the CARS signal near 496 nm before the signal was guided to the spectrometer using dichroic long-pass mirrors (cut-off at 550 nm). In addition, a short-pass filter at 550 nm and a notch filter at 532 nm were used to eliminate residual reflections at the pump wavelengths. Depending on the temperature, neutral density filters were used to prevent saturation of the detection camera. Before focusing the CARS signal into the spectrometer (SPEX Industries Inc., 1704, 1m, 2400 lpmm) with a  $f = 100$  mm focusing lens, an achromatic half-wave retardation plate was used to rotate the polarization for optimal dispersion at the grating. A cooled back-light illuminated CCD (Princeton Instruments, Pixis 400) captured the dispersed signal. The readout area was limited to 25 px in height which were hardware binned to obtain a one-dimensional spectrum. The camera was operated at 20 Hz to allow capturing an intermediate background frame between laser shots to correct for dark current. The spectral profile of the Stokes laser was accounted for by normalizing the CARS spectra to a non-resonant signal acquired in Argon at regular intervals during the day.

After background correction and normalization to the non-resonant signal, the CARS spectra were processed using our in-house spectral fitting algorithm<sup>4</sup> to obtain the temperature and  $CO_2$  mole fraction from single-shot spectra. The algorithm is an extension of our previously published approach for single-pump  $N_2$  CARS spectra based on lossless compressed libraries (Greifenstein and Dreizler 2021b). The underlying model for  $N_2$  is described therein, while the  $CO_2$  model of CARSFT (Palmer 1989) was used which is based on the approach published by Hall and Stufflebeam

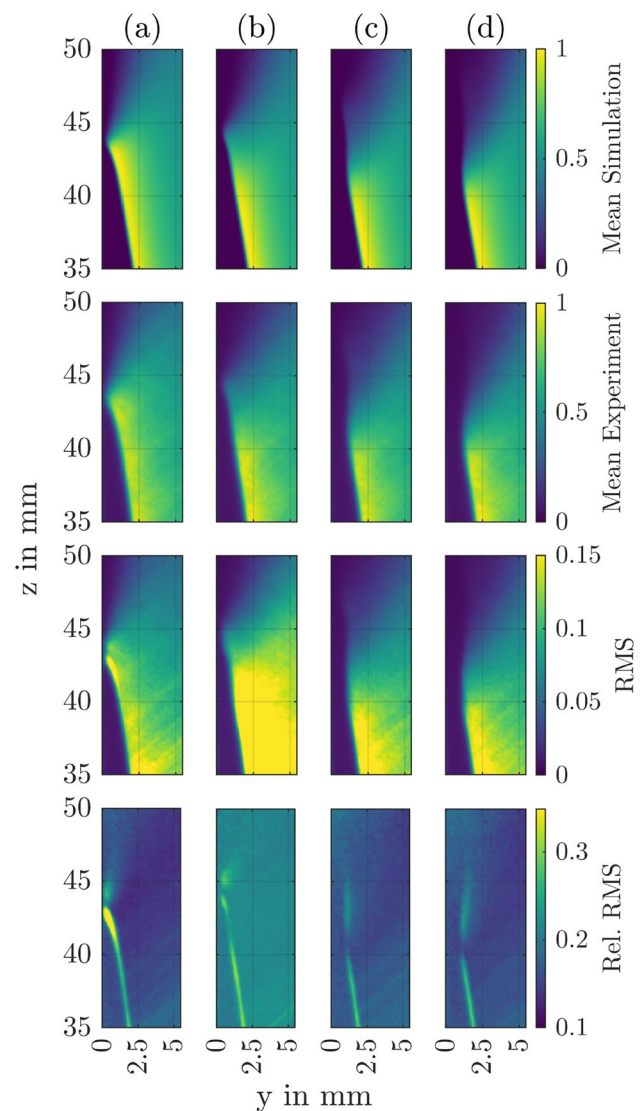


**Fig. 3** Comparison of simulated OH-PLIF signal and experimentally obtained OH-PLIF signal for boundary layer flames (a)–(d)

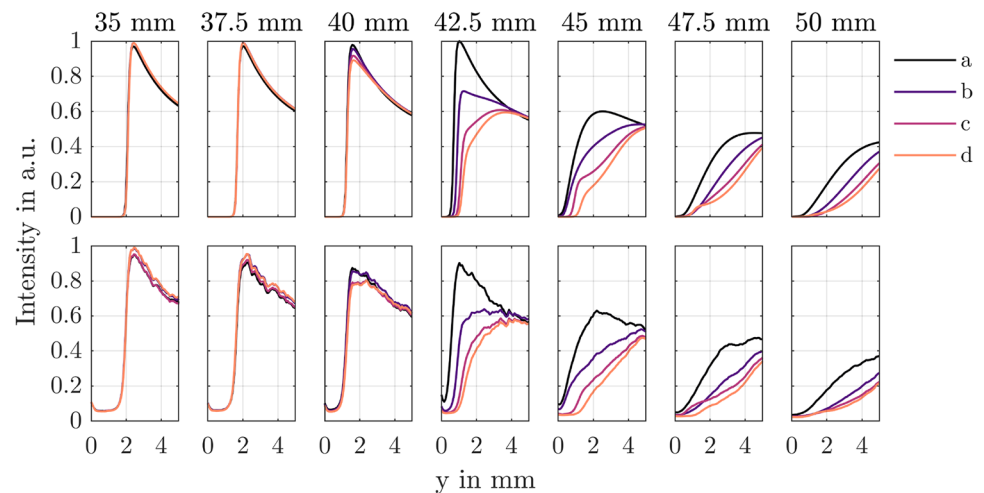
(1984). Based on measurements in the free flame branch, the  $CO_2$  mole fraction deviates by  $\approx 8\%$  with a precision of  $\approx 15\%$ . For the temperature evaluation,  $\approx 6\%$  and  $\approx 2.5\%$  are reported.

### 3 Results and discussion

The presentation of discussion and results for the study is split into three parts: At first, simulated and measured OH-PLIF data are compared to provide a first insight on the agreement between these approaches and to guide the reader through the subsequent sections. These cover a discussion on the local mixing field based on the NO-tracer-PLIF measurements followed by discussing the influence of different

<sup>4</sup> Publication currently under review.

**Fig. 4** Comparison of wall-normal OH-LIF profiles at various heights. Top row: simulation, bottom row: experiment



degrees of partial premixing on the local thermochemical states near the quenching wall.

### 3.1 OH-PLIF

The mean, RMS and relative RMS of the experimentally measured OH-PLIF images of the boundary layer flames are presented in Fig. 3 together with the simulation result. For this comparison, the numerical simulation incorporated a simulated OH-LIF signal routine as described by Popp et al. (2015) and Kosaka et al. (2020), taking into account local quenching rates and temperature dependent variation in Boltzmann fraction. The signals are normalized to the respective peak value inside the field of view, which is located within the reaction zone. The shown field of view begins right above the effusive wall inlet at 35.5 mm and extends vertically over a distance of 15 mm. As the simulation does not include the near-nozzle area, a matching of the vertical coordinate is required to compare experimental and numerical data. This is achieved by fitting the numerical data to the experimental data for the reference case (a) by means of a nonlinear least squares fit using only the  $z$ -coordinate as a parameter. This mapping was used for all cases (a)–(d).

With increasing secondary fuel mass flow through the effusive inlet for cases (a)–(b), the mean OH-PLIF signal exhibits an apparent downstream shift of the quenching location. For cases (c) and (d), characterized by the highest secondary fuel inflows through the effusive inlet, a distinct quenching point cannot be identified due to the enrichment of partially premixed gas upstream of the reaction zone. This local enrichment causes a strong shift in the OH-CO reaction pathway, favoring locally higher CO and lower OH concentrations. This leads to a strong reduction in the OH gradient which no longer correlates with the location of the highest heat release rates due to the formation of a concentration

boundary layer with enriched mixture (Steinhausen et al. 2022).

The RMS and RMS after normalization to the local mean (Rel. RMS in Fig. 3) obtained from the experimental samples exhibit the highest values near the reaction zone, consistent with previous measurements (Jainski et al. 2017). These fluctuations are attributed to Helmholtz-type resonances within the burner, causing spatial fluctuations in the order of  $\pm 200 \mu\text{m}$ . In other words, even though the flame is laminar, it is not perfectly stationary.

Overall, there is excellent agreement between the numerical simulation and the experiment. The key features such as the shift of the apparent quenching location with increasing secondary fuel mass flow and the development of a buffer layer with low OH signal intensity upstream of the inlet observed in the experiment are well captured in the simulation.

For a more detailed comparison, Fig. 4 shows wall-normal profiles of the normalized OH LIF intensity extracted every 2.5 mm from the field of view shown in Fig. 3. Due to inhomogeneities in the laser sheet and the normalization of the entire image to the peak values, the peak intensity for the extracted profiles drops to values  $< 1$  for higher axial

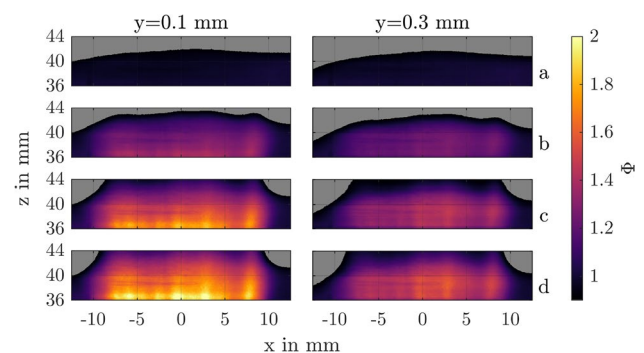


**Fig. 5** Experimentally obtained wall parallel equivalence ratios. The effusive inlet is located between 30.5 and 35.5 mm



**Fig. 6** Wall-parallel in horizontal direction of measured equivalence ratios for all cases. Dash-dotted lines in the left plot show the local equivalence ratio for cases b and c without correcting for absorption effects

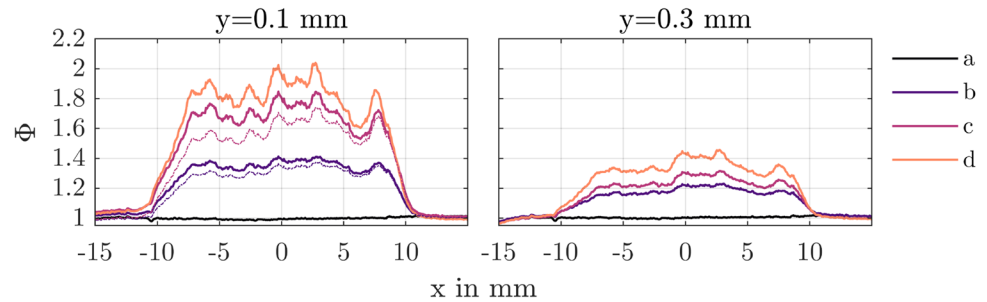
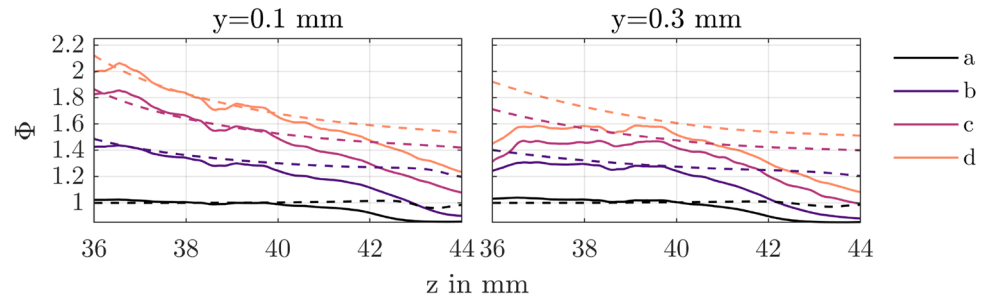


**Fig. 7** Comparison of wall-parallel profiles of the local equivalence ratio at two different wall-distances. Solid lines: experiment, dashed lines: simulation



coordinates. Moreover, residual reflections and limited spatial resolution of the used image intensifier cause the experimentally obtained OH LIF signal to exhibit values  $> 0$  near the wall. Despite these experimental artifacts, the agreement between numerical simulation and experiment is excellent, accurately capturing the lowering of the OH signal intensity and wall-normal gradient with increasing secondary inflow. However, close to the quenching point near 45 mm, the simulation predicts a steep near step-like increase within the first 1–2 mm for cases (c) and (d) which appear not as dominant in the experiment. Some residue of this effect is still visible even at 47.5 mm. This might indicate that the local mixing field close to the wall is not accurately captured in the numerical simulation. As will later be seen, this is very likely due to spatial inhomogeneities in the outflow of the effusive wall inlet, making a direct comparison in this area solely based on the OH LIF signal intensity challenging. In this area, the mixing field is strongly influenced by the local momentum ratio of the primary flow through the burner nozzle and the secondary inflow through the effusive inlet. Due to the comparably low secondary volumetric flow rate, the secondary flow field penetrates only into the boundary layer. As such, the local mixing field is strongly influenced by accurately capturing the near wall velocity gradient. This aspect and the issue with inhomogeneities within the secondary inflow due to spatial variation of local porosity in the sintered material will be further addressed in the following section.

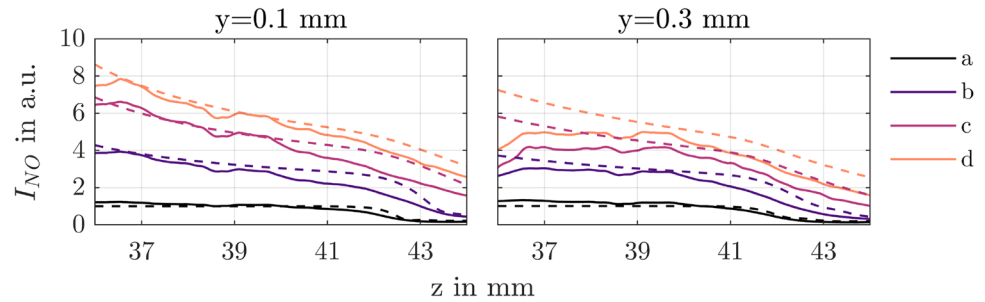
### 3.2 Local equivalence ratio

Figure 5 shows the measured equivalence ratio between the effusive inlet and the downstream reaction zone for wall distances  $y = 0.1$  mm and  $y = 0.3$  mm for all measured cases. Due to the increase in temperature, the NO-LIF data are only evaluated  $\approx 2$  mm upstream of the reaction zone. The increase in secondary fuel inflow leads to a locally richer mixture and a vertical shift of the reaction zone, indicating a retardation of the reaction process which is expected when starting the enrichment from a stoichiometric mixture. Clearly visible is the aforementioned inhomogeneity of the outflow in  $x$ -direction. Although not visible in this wall-parallel orientation, an additional inhomogeneity in  $z$  direction has to be considered. Regardless of the inhomogeneities, the local equivalence ratio is reduced both increasing with axial coordinate and wall distance.

Figure 6 shows wall-parallel line plots extracted at  $z = 36$  mm. For a wall-distance of  $y = 0.3$  mm, the absorption correction yields very accurate results, as the measured local equivalence ratio is very close to 1 in the wings of the profiles, where no secondary flow penetrates the primary mixture. For  $y = 0.1$  mm, a slight overcompensation is observed, leading to  $\Phi \approx 1.05$  where a value of 1 is expected. The mentioned inhomogeneities become very apparent in this presentation. Between  $x = -6$  mm and 6 mm, the variation increases from 10% for case (b) to 20% for case (d) (min–max) for the profiles closest to the quenching wall.

To compare the numerical simulation and experimental data, Fig. 7 shows wall-parallel profiles of the local equivalence ratio in vertical direction extracted at  $x = 0$  mm for both measured wall-distances for all cases. Up to  $z = 40$  mm, the data are in excellent agreement for  $y = 0.1$  mm. For  $y = 0.3$  mm, the

**Fig. 8** Comparison of wall-parallel profiles of the measured NO-LIF signal and the simulated NO-LIF signal. Solid lines: experiment, dashed lines: simulation



**Fig. 9** LIF signal comparison for case c with varying inflow velocity boundary condition (1x, 2x, 4x) in simulation

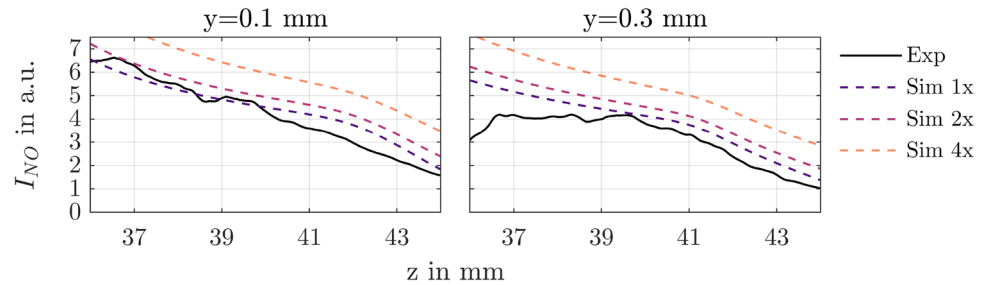
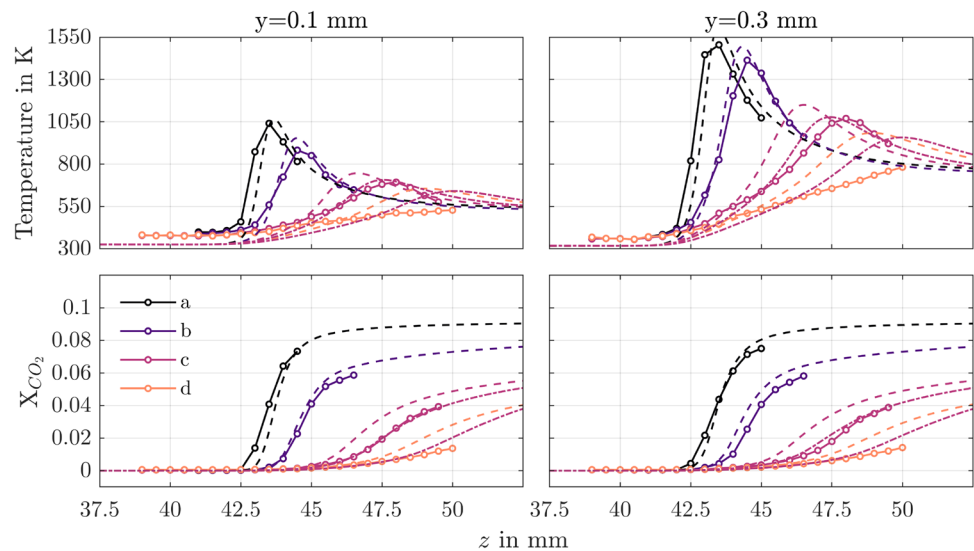


**Fig. 10** Wall-parallel temperature (top row) and CO<sub>2</sub> mole fraction (bottom row) profiles at two different wall-distances. Solid lines: experiment, dashed lines: simulation. For case (c), the sensitivity study of the outflow velocities is shown as dashed (1x) and dash-dotted lines (2x, 4x)



experimentally obtained profiles exhibit a plateau in the local equivalence ratio which is not present in the simulation. It is assumed that the penetration depth in the experiment at this location is lower compared to the simulation due to uncertainties in the local flow rate and potentially inaccuracies in the boundary layer velocity gradient near the effusive inlet. Possibly, this could be caused by a disturbance in the boundary layer arising from a not perfectly flush-mounted inlet. This could potentially lead to a local recirculation, impeding the penetration depth of the secondary fuel inflow. As the inflow is assumed to be homogenous across the surface area of the effusive inlet in the numerical simulation, a direct comparison is very challenging.

For measurements further downstream at  $z > 40$  mm, the deviation is mostly explained by the increase in temperature

as the vertical coordinate approaches the reaction zone. This assumption is verified by simulating the NO-LIF signal in the numerical simulation and comparing this quantity with the uncalibrated absorption corrected NO-PLIF signal from the experiment. In contrast to comparing the local equivalence ratio directly, this comparison, shown in Fig. 8, has the benefit of omitting the assumption that the locally measured NO signal correlates with the local equivalence ratio. This rules out potentially different diffusive fluxes of NO and CH<sub>4</sub>. This is motivated by the notion that even though the diffusion coefficient of these species is very similar, the concentration gradient may not be equal, resulting in differential diffusion effects. For this presentation, the simulated and measured LIF signals are normalized to 1 for case (a) at  $z = 40$  mm. Here, a decent agreement

in the decline of the profiles with increasing axial coordinate is observed, albeit with the same plateau in the experiment at  $y = 0.3$  mm which is not present in the simulation. This shows that differential diffusion effects can be neglected.

In order to test the sensitivity of the inhomogeneities, numerical simulations with varying outlet velocities (1x, 2x, 4x the nominal value) for the secondary fuel flow were carried out for case (c). Figure 9 shows this comparison together with the measured LIF signal after preprocessing. As expected, a higher outlet velocity leads to an increased simulated NO LIF signal and also to higher local equivalence ratios. However, the net effect of doubling the nominal outflow velocity is less pronounced than one might expect due to the diffusive nature of the process. The experimentally measured profile for  $z \leq 40$  mm at  $y = 0.1$  mm lies well between the simulated profiles, indicating a comparably low sensitivity of the local mixing state near the quenching wall to the convective flux of the outflow.

### 3.3 Thermochemical state

In this section, the influence of partial premixing on the local gas phase temperature and  $\text{CO}_2$  mole fraction in physical coordinates and state space is discussed. Figure 10 shows the comparison of experimentally and numerically obtained wall-parallel profiles of temperature and  $\text{CO}_2$  mole fraction for all cases at both investigated wall distances.

As can be seen for the reference case (a) without secondary fuel inflow, the agreement between simulation and experiment is excellent, albeit with an apparent vertical shift by  $\Delta z \approx 200$   $\mu\text{m}$ . This is likely due to an uncertainty in the matching procedure of the vertical axis based on the OH-PLIF signal due to the limited spatial resolution of the detection system. Comparing cases (b)–(d) with the nominal outflow velocity, i.e., assuming a uniform outflow across the surface area of the effusive inlet, both temperature and  $\text{CO}_2$  mole fraction rise prematurely, with a higher gradient and to higher end values in the simulation. The variation of the outflow velocity shows a very good agreement between the experimentally and numerically obtained wall-parallel temperature and  $\text{CO}_2$  mole fraction profiles when a twofold increase in the outflow velocity is used in the simulation. Indeed, near  $x = 0$  mm, where the CARS measurement volume is located, the mixture is richer than the average value due to the inhomogeneities of the inlet, see Fig. 5. As the temperature and  $\text{CO}_2$  profiles match very well and the sensitivity of the LIF signal to a twofold increase in outlet velocity is within the experimental accuracy of the LIF measurement, it is reasonable to assume that the discrepancies between simulation and experiment are entirely caused by the inhomogeneities in the effusive inlet. This notion is further verified when plotting the data in state space, see Fig. 11. Reference case (a) shows—as expected from the spatial profiles—excellent agreement. For cases (b)–(d), an increasing overprediction of temperature and  $\text{CO}_2$  is observed in the numerical simulations when using the

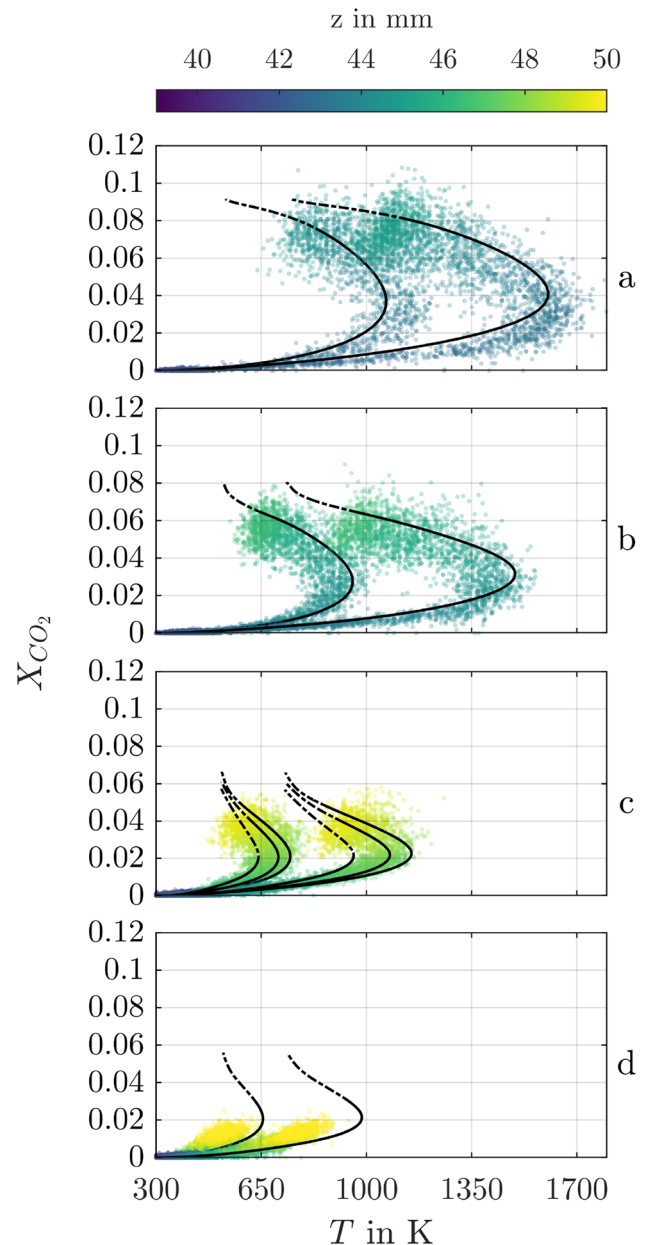


**Fig. 11** Thermochemical state scatter plots for cases (a)–(d) from top to bottom. Color for the experimental data indicates  $z$  coordinate. Black lines: simulation. Transition to dashed line at highest  $z$  coordinate of the corresponding experiment. For case (c), three simulations with varying inflow velocity are shown for each wall distance. From right to left: 1x, 2x, 4x

nominal outflow velocity, neglecting local inhomogeneities. The variation of the outflow velocity for case (c) shows again a reasonable agreement when using a twofold increase.

The thermochemical state is severely altered by the presence of a secondary inflow. With increasing flowrate of secondary fuel, the thermochemistry is shifted toward lower temperatures and lower  $\text{CO}_2$  mole fractions. This indicates

a strong retardance of chemical time scales due to reduced heat release rates caused by the local enrichment.

## 4 Conclusion

Within this study, we investigated the local thermochemical state and equivalence ratio in a canonical, vertically oriented partially premixed boundary layer flame under laminar flow conditions. Partial-premixing was achieved by implementing a secondary methane inflow through an effusive element embedded in the wall. The volumetric flow rate through this effusive inlet was varied to mimic different pyrolysis rates of a wall-embedded polymer under well-controlled boundary conditions and reduced chemical complexity. The established boundary layer flames were investigated using coherent anti-Stokes Raman spectroscopy for the gas phase temperature and CO<sub>2</sub> mole fraction. Simultaneously, NO was seeded into the primary as well as the secondary flow to measure the local equivalence ratio using planar laser-induced fluorescence. Additionally, planar OH-LIF was used in the experiments to capture the reaction zone location.

This study provides insights into the very complex interplay between mixing and heat loss, which is a challenging combination to capture in numerical simulations. The dominant source of uncertainty is the inhomogeneity of the effusive inlet due to local variations of porosity, leading to locally different flow velocities. Overall, an excellent agreement between numerical

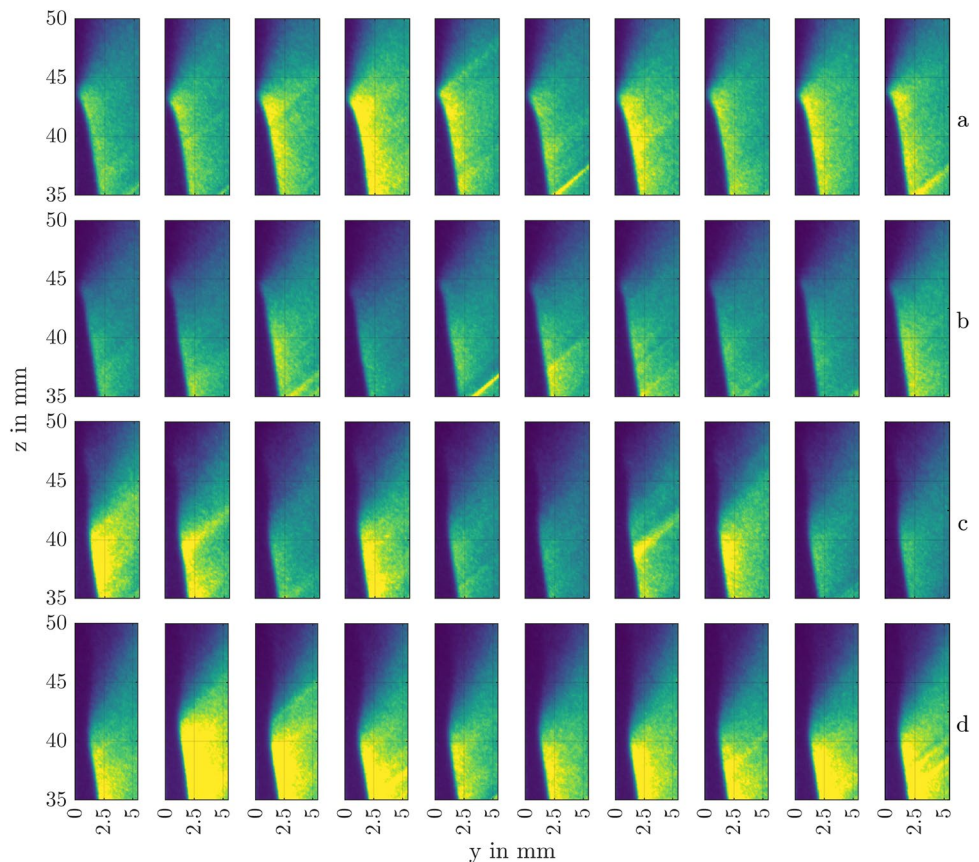
simulations and experiment was obtained, when accounting for these inhomogeneities.

According to the measurements and simulations, the local equivalence ratios 2 mm upstream of the reaction zone reach values of up to  $\Phi \approx 2$ . For these conditions, a quenching location that is typically found in this side-wall quenching configuration cannot be inferred from OH-PLIF measurements due to the shift in OH-CO equilibrium for fuel-rich flames. This statement is supported by the simulation, which predicts higher CO concentrations near the temperature-controlled wall for higher secondary fuel flow rates. However, this has to be verified experimentally. The thermochemical state shows a significant change toward lower temperatures and lower CO<sub>2</sub> mole fractions. This indicates longer chemical time scales due to lower local heat release rates. For a hypothetical vertically oriented wall-embedded polymer, this effect is likely to cause a spatial variation of pyrolysis rates with its height. As the wall-embedded polymer is likely to ignite at the bottom first, the ongoing fuel-rich combustion of its pyrolysis products will lead to a negative temperature gradient in vertical direction, locally retarding the pyrolysis rates. This hypothesis, formulated based on the data presented in this study, will be further investigated in future publications.

## Appendix

See Fig. 12.

Fig. 12 OH LIF single shots



**Author contributions** M.G. and F.Z. and P.J.: Design and conduction of experiments. M.S.: Numerical modeling and simulation. M.G.: Evaluation of experimental data; Code writing; drafting of original manuscript; figure preparation; B.B., A.D., C.H.: Conceptualization, Supervision, Funding acquisition, Project administration, Resources; All authors reviewed the manuscript.

**Funding** Open Access funding enabled and organized by Projekt DEAL. This project is funded by the Deutsche Forschungsgemeinschaft (DFG, German Research Foundation) Projektnummer 237267381 TRR 150.

**Data availability statement** If this manuscript will be accepted for publication, the data presented in the final version of the manuscript will be hosted in our university's public data repository TU Datalib.

**Code availability** A custom code was developed and used for all data processing presented in this manuscript.

## Declarations

**Conflict of interest** The authors declare that they have no conflict of interest.

**Open Access** This article is licensed under a Creative Commons Attribution 4.0 International License, which permits use, sharing, adaptation, distribution and reproduction in any medium or format, as long as you give appropriate credit to the original author(s) and the source, provide a link to the Creative Commons licence, and indicate if changes were made. The images or other third party material in this article are included in the article's Creative Commons licence, unless indicated otherwise in a credit line to the material. If material is not included in the article's Creative Commons licence and your intended use is not permitted by statutory regulation or exceeds the permitted use, you will need to obtain permission directly from the copyright holder. To view a copy of this licence, visit <http://creativecommons.org/licenses/by/4.0/>.

## References

- Ananth R, Ndubizu CC, Tatem P (2003) Burning rate distributions for boundary layer flow combustion of a PMMA plate in forced flow. *Combust Flame* 135(1–2):35–55
- Annamalai K, Sibulkin M (1979) Flame spread over combustible surfaces for laminar flow systems part I: excess fuel and heat flux. *Combust Sci Technol* 19(5–6):167–183
- Atakan B, Heinze J, Meier UE (1997) OH laser-induced fluorescence at high pressures: spectroscopic and two-dimensional measurements exciting the A-X (1,0) transition. *Appl Phys B Lasers Opt* 64(5):585–591. <https://doi.org/10.1007/s003400050219>
- Bessler WG, Schulz C, Lee T, Jeffries JB, Hanson RK (2002) Strategies for Laser-induced Fluorescence Detection of Nitric Oxide in High-pressure flames. I. A-X excitation. *Appl Opt* 41(18):3547–3557
- Bessler WG, Schulz C, Sick V, Daily JW (2003) A versatile modeling tool for nitric oxide LIF spectra. In: Proceedings of the third joint meeting of the US sections of the combustion institute, vol 3
- Coffee T, Heimerl J (1981) Transport algorithms for premixed, laminar steady-state flames. *Combust Flame* 43:273–289
- Consalvi J, Porterie B, Coutin M, Audouin L, Casselman C, Rangwala A, Buckley S, Torero J (2005) Diffusion flames upwardly propagating over PMMA: theory, experiment and numerical modeling. *Fire Saf Sci* 8:397–408
- Consalvi JL, Pizzo Y, Porterie B (2008) Numerical analysis of the heating process in upward flame spread over thick PMMA slabs. *Fire Saf J* 43(5):351–362
- Creative Commons (2013) Creative commons attribution license CC BY 4.0. <http://creativecommons.org/licenses/by/4.0/>
- Curtiss CF, Hirschfelder JO (1949) Transport properties of multicomponent gas mixtures. *J Chem Phys* 17(6):550–555
- De Ris J, Markstein G, Orloff L, Beaulieu P (2003) Similarity of turbulent wall fires. *Fire Saf Sci* 7:259–270
- Drysdale D (2011) An introduction to fire dynamics. Wiley, London
- Emmons H (1956) The film combustion of liquid fuel. *ZAMM J Appl Math Mech* 36(1–2):60–71
- Greifenstein M, Dreizler A (2021a) Investigation of mixing processes of effusion cooling air and main flow in a single sector model gas turbine combustor at elevated pressure. *Int J Heat Fluid Flow* 88:108768
- Greifenstein M, Dreizler A (2021b) Marsft: Efficient fitting of cars spectra using a library-based genetic algorithm. *J Raman Spectrosc* 52(3):655–663
- Hall RJ, Stufflebeam JH (1984) Quantitative cars spectroscopy of CO<sub>2</sub> and N<sub>2</sub>O. *Appl Opt* 23(23):4319–4327
- Heinze J, Meier U, Behrendt T, Willert C, Geigle KP, Lammel O, Lücknerath R (2011) PLIF thermometry based on measurements of absolute concentrations of the OH radical. *Z Phys Chem* 225(11–12):1315–1341. <https://doi.org/10.1524/zpch.2011.0168>
- Hirano T (1972) Measurement of the velocity distribution in the boundary layer over a flat plate with a diffusion flame. *Astronaut Acta* 17:811–818
- Hirano T, Kanno Y (1973) Aerodynamic and thermal structures of the laminar boundary layer over a flat plate with a diffusion flame. In: Symposium (international) on combustion. Elsevier, vol 14, pp 391–398
- Jainki C, Ribmann M, Böhm B, Janicka J, Dreizler A (2017) Sidewall quenching of atmospheric laminar premixed flames studied by laser-based diagnostics. *Combust Flame* 183:271–282
- Kennedy LA, Plumb O (1977) Prediction of buoyancy controlled turbulent wall diffusion flames. In: Symposium (international) on combustion. Elsevier, vol 16, pp 1699–1707
- Kosaka H, Zentgraf F, Scholtissek A, Bischoff L, Häber T, Suntz R, Albert B, Hasse C, Dreizler A (2018) Wall heat fluxes and CO formation/oxidation during laminar and turbulent side-wall quenching of methane and DME flames. *Int J Heat Fluid Flow* 70:181–192
- Kosaka H, Zentgraf F, Scholtissek A, Hasse C, Dreizler A (2020) Effect of flame-wall interaction on local heat release of methane and DME combustion in a side-wall quenching geometry. *Flow Turbul Combust* 104:1029–1046
- Krishnamurthy L, Williams F (1973) On the temperatures of regressing PMMA surfaces. *Combust Flame* 20(2):163–169
- Luque J, Crosley D (1999) LIFBASE: database and simulation program (v 2.1.1). SRI International Report MP, pp 99–009. <https://www.sri.com/engage/products-solutions/lifbase>
- Mell WE, Kashiwagi T (1998) Dimensional effects on the transition from ignition to flame spread in microgravity. In: Symposium (international) on combustion. Elsevier, vol 27, pp 2635–2641
- Mell WE, Kashiwagi T (2000) Effects of finite sample width on transition and flame spread in microgravity. *Proc Combust Inst* 28(2):2785–2792
- Nakamura Y, Kashiwagi T, McGrattan KB, Baum HR (2002) Enclosure effects on flame spread over solid fuels in microgravity. *Combust Flame* 130(4):307–321
- Orloff L, Modak AT, Alpert R (1977) Burning of large-scale vertical surfaces. In: Symposium (international) on combustion. Elsevier, vol 16, pp 1345–1354

- Palmer R (1989) The CARSFT computer code calculating coherent anti-stokes Raman spectra: user and programmer information. Technical report, Sandia National Labs., Livermore, CA (USA)
- Paul P (1997) Calculation of transition frequencies and rotational line strengths in the  $\gamma$ -bands of nitric oxide. *J Quant Spectrosc Radiat Transf* 57(5):581–589
- Popp S, Hunger F, Hartl S, Messig D, Coriton B, Frank JH, Fuest F, Hasse C (2015) Les flamelet-progress variable modeling and measurements of a turbulent partially-premixed dimethyl ether jet flame. *Combust Flame* 162(8):3016–3029
- Raghavan V, Rangwala A, Torero J (2009) Laminar flame propagation on a horizontal fuel surface: verification of classical Emmons solution. *Combust Theor Model* 13(1):121–141
- Ren N, Wang Y, Vilfayeau S, Trouvé A (2016) Large eddy simulation of turbulent vertical wall fires supplied with gaseous fuel through porous burners. *Combust Flame* 169:194–208
- Sadanandan R, Fleck J, Meier W, Griebel P, Naumann C (2012a) 2D mixture fraction measurements in a high pressure and high temperature combustion system using NO tracer-LIF. *Appl Phys B* 106(1):185–196
- Sadanandan R, Meier W, Heinze J (2012b) Experimental study of signal trapping of OH laser induced fluorescence and chemiluminescence in flames. *Appl Phys B* 106(3):717–724. <https://doi.org/10.1007/s00340-011-4704-z>
- Settersten TB, Patterson BD, Humphries WH IV (2009) Radiative lifetimes of NO  $A^2\Sigma^+$  ( $v' = 0, 1, 2$ ) and the electronic transition moment of the  $A^2\Sigma^+ - X^2\Pi$  system. *J Chem Phys* 131(10):104309
- Shih HY, James S (2003) A three-dimensional model of steady flame spread over a thin solid in low-speed concurrent flows. *Combust Theor Model* 7(4):677
- Shih HY, Tien JS (2000) Modeling concurrent flame spread over a thin solid in a low-speed flow tunnel. *Proc Combust Inst* 28(2):2777–2784
- Singh AV, Gollner MJ (2015) A methodology for estimation of local heat fluxes in steady laminar boundary layer diffusion flames. *Combust Flame* 162(5):2214–2230
- Skalska K, Miller J, Ledakowicz S (2010) Kinetics of nitric oxide oxidation. *Chem Pap* 64(2):269–272
- Smith GP, Golden DM, Frenklach M, Moriarty NW, Eiteneer B, Goldenberg M, Bowman CT, Hanson RK, Song S, Gardiner Jr W et al (2011) GRI-Mech 3.0. [http://www.me.berkeley.edu/gri\\_mech](http://www.me.berkeley.edu/gri_mech)
- Steinhausen M, Luo Y, Popp S, Strassacker C, Zirwes T, Kosaka H, Zentgraf F, Maas U, Sadiki A, Dreizler A et al (2021) Numerical investigation of local heat-release rates and thermo-chemical states in side-wall quenching of laminar methane and dimethyl ether flames. *Flow Turbul Combust* 106:681–700
- Steinhausen M, Ferraro F, Schneider M, Zentgraf F, Greifenstein M, Dreizler A, Hasse C, Scholtissek A (2022) Effect of flame retardants on side-wall quenching of partially premixed laminar flames. In: Proceedings of the combustion institute
- Stroh A, Hasegawa Y, Schlatter P, Frohnapfel B (2016) Global effect of local skin friction drag reduction in spatially developing turbulent boundary layer. *J Fluid Mech* 805:303–321
- Tamanini F (1979) A numerical model for the prediction of radiation-controlled turbulent wall fires. In: Symposium (international) on combustion. Elsevier, vol 17, pp 1075–1085
- Wang HY, Coutin M, Most JM (2002) Large-eddy-simulation of buoyancy-driven fire propagation behind a pyrolysis zone along a vertical wall. *Fire Saf J* 37(3):259–285
- Zentgraf F (2022) Investigation of reaction and transport phenomena during flame-wall interaction using laser diagnostics. Ph.D. thesis, Technische Universität Darmstadt
- Zentgraf F, Johe P, Cutler AD, Barlow RS, Boehm B, Dreizler A (2022a) Classification of flame prehistory and quenching topology in a side-wall quenching burner at low-intensity turbulence by correlating transport effects with  $\text{CO}_2$ , CO and temperature. *Combust Flame* 239:111681
- Zentgraf F, Johe P, Steinhausen M, Hasse C, Greifenstein M, Cutler AD, Barlow RS, Dreizler A (2022b) Detailed assessment of the thermochemistry in a side-wall quenching burner by simultaneous quantitative measurement of  $\text{CO}_2$ , CO and temperature using laser diagnostics. *Combust Flame* 235:111707
- Zhou L, Fernandez-Pello A (1992) Solid fuel combustion in a forced, turbulent, flat plate flow: the effect of buoyancy. In: Symposium (international) on combustion. Elsevier, vol 24, pp 1721–1728
- Zhou L, Fernandez-Pello A (1993) Turbulent, concurrent, ceiling flame spread: the effect of buoyancy. *Combust Flame* 92(1–2):45–59

**Publisher's Note** Springer Nature remains neutral with regard to jurisdictional claims in published maps and institutional affiliations.

## Authors and Affiliations

M. Greifenstein<sup>1</sup> · F. Zentgraf<sup>1</sup> · P. Johe<sup>1</sup> · B. Boehm<sup>1</sup> · M. Steinhausen<sup>2</sup> · C. Hasse<sup>2</sup> · A. Dreizler<sup>1</sup>

✉ M. Greifenstein  
greifenstein@rsm.tu-darmstadt.de

<sup>1</sup> Department of Mechanical Engineering, Reactive Flows and Diagnostics, Technical University of Darmstadt, Otto-Berndt-Str. 3, 64287 Darmstadt, Germany

<sup>2</sup> Department of Mechanical Engineering, Simulation of reactive Thermo-Fluid Systems, Technical University of Darmstadt, Otto-Berndt-Str. 2, 64287 Darmstadt, Germany